Electronic Supplementary Information (ESI) for:

In situ Environmental TEM Observation of Two-stage Shrinking of Cu_2O Islands on Cu(100) during Methanol Reduction

Hao Chi[1], Matthew T. Curnan[1], Meng Li[1], Christopher M. Andolina[1], Wissam A. Saidi[2], Götz Veser[1, 3], Judith C. Yang[1, 4]

[1]*Department of Chemical and Petroleum Engineering, University of Pittsburgh, Pittsburgh, PA 15216, USA*
[2] *Department of Chemical and Petroleum Engineering, University of Pittsburgh, Pittsburgh, PA 15216, USA*
[3] *Center for Energy, University of Pittsburgh, PA 15216, USA*
[4] *Department of Physics, University of Pittsburgh, Pittsburgh, PA 15216, USA*

ESI Contents

Movie S1. Reduction of Cu_2O nano-island on Cu(100) support at 250°C under 7.6×10^{-6} Torr MeOH vapor showing shrinking of entire island.

Movie S2. Reduction of Cu_2O nano-island on Cu(100) support at 250°C under 7.6×10^{-6} Torr MeOH vapor showing evolution of Cu_2O(110) lattice fringes.

Note 1: Methods

Multiple single-crystalline Cu(100) films used in this work were produced by *e*-beam evaporation of 99.999% pure Cu pellets on NaCl(100) substrates. The films were grown in a UHV evaporator system with an approximate base pressure of 1×10^{-9} Torr. The deposition rate was measured by quartz crystal thickness monitors and the NaCl substrate was heated by *e*-beam with a temperature stability of ±5 K. Cu(100) thin films were epitaxially grown on the NaCl(100) substrate, with a deposition rate of 1.2 Å/s and a substrate temperature of 300 °C, to grow 60 nm thick Cu films. The NaCl substrate was dissolved in deionized water (Milli-Q, 18.2 MΩ.cm) and then the Cu films were then floated onto Cu TEM mesh grids. A differentially pumped ETEM (Hitachi H-9500) running at 300 keV, equipped with a double-tilt heating holder and home-made gas injection system, was used in this study. The ETEM was evacuated to a base vacuum of 10^{-4} Pa. Real-time TEM videos and images were recorded by an Orius SC1000A camera at a frame rate of 5 frames/s.

All useable frames of videos are aligned to compensate for thermal drift and were measured using Fiji ImageJ. The dimensions of the island throughout the movie are measured by extracting kymograph measurements of the island along a horizontal ($2r$) and vertical (h) line. In the kymograph measurements, each pixel along the vertical direction corresponds to one frame, which can be converted to time based on the frame rate of the movie. Each pixel along the horizontal direction corresponds to the feature in the movie along the scanned line at the corresponding frame, so the horizontal direction pixels can be converted to dimensions based on the scale bar of the movie. Feature detection was then performed to get the shape of the Cu_2O island in the kymograph, namely based on the contrast differences between Cu_2O, Cu, and vacuum in the frames. Measurement of the island dimensions was then performed by calculating the lengths of the detected features in each horizontal line. Further explanation of matching approaches can be found in past work.[31]

The native oxide (Cu_2O) on Cu films was removed via H_2 exposures *in situ* at a partial pressure of 7.6×10^{-6} Torr and 650 °C. The elevated temperature annealing also facilitates the formation of faceted holes – with (100) and (110) facets – on Cu films, which enables ensuing observation of Cu_2O nano-island reduction from the edge-on view. H_2 was then pumped out of the microscope. Second, Cu_2O nano-islands were grown under an O_2 partial pressure of $P_{O2} = 1.5\times10^{-4}$ Torr and $T = 350$ °C for ~5 min, which is a typical condition for Cu_2O nano-island growth. In order to observe the subsequent reduction of Cu_2O under MeOH, O_2 is pumped away and then MeOH vapor is introduced into the specimen chamber controlled by a needle valve. *In situ* TEM observation of Cu_2O reductive shrinking is carried out by imaging the overall Cu_2O nano-island geometry under MeOH vapor at 7.6×10^{-6} Torr and 250 °C.

To rule out any geometric change induced solely by *e*-beam, the Cu_2O nano-islands were observed under relatively low beam intensities and under lower magnification. Hence, movie and image quality in this work may be lower than other published movies and images produced by this ETEM. Before MeOH injection, each island was illuminated under vacuum condition for 5 min. No significant geometric change of Cu_2O was captured during this period, which diminishes the possibility of *e*-beam effects impacting Cu_2O island shrinking. In comparison, all of our reported Cu_2O nano-islands can be reduced completely by MeOH within 3 min.

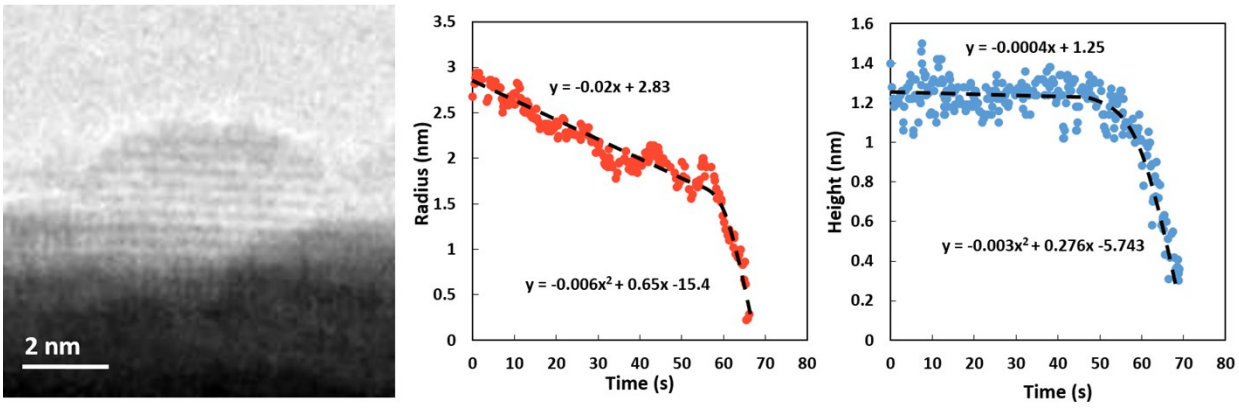

Figure S1. Shrinking profile of Cu_2O island (#1 in Table S8) with fitting parameters**.**

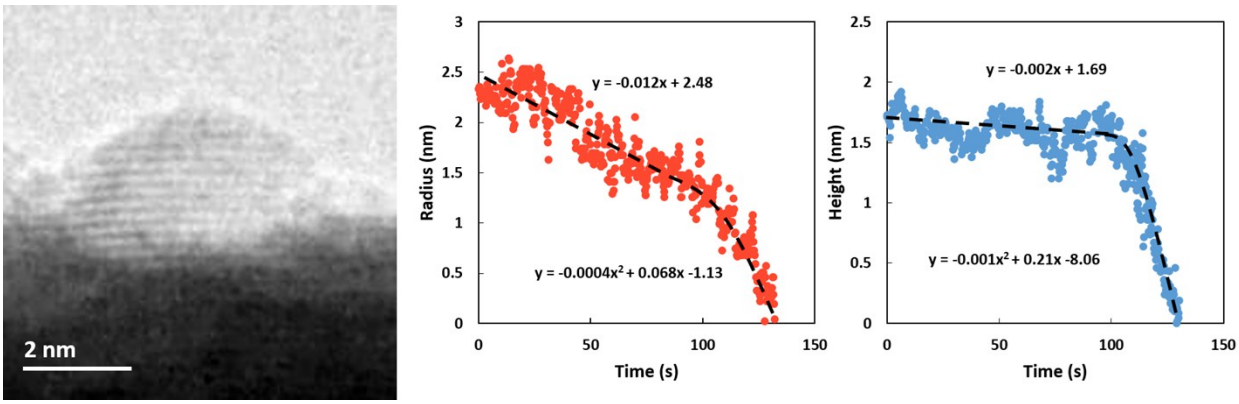

Figure S2. Shrinking profile of Cu_2O island (#2 in Table S8) with fitting parameters.

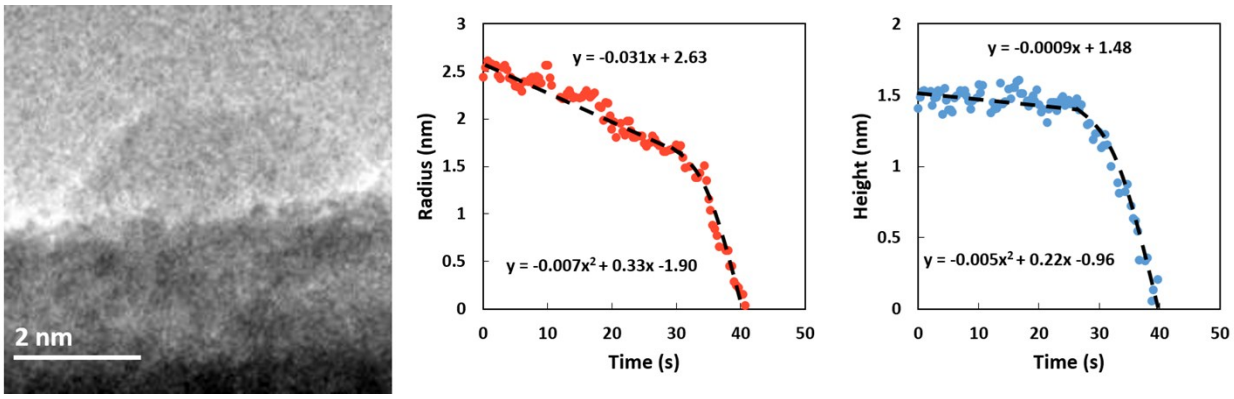

Figure S3. Shrinking profile of Cu_2O island (#3 in Table S8) with fitting parameters**.**

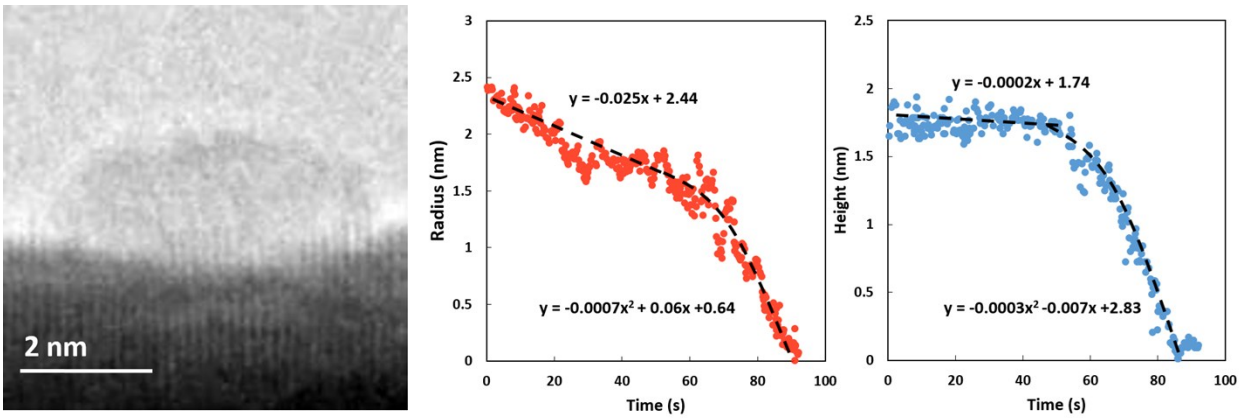

Figure S4. Shrinking profile of Cu_2O island (#4 in Table S8) with fitting parameters.

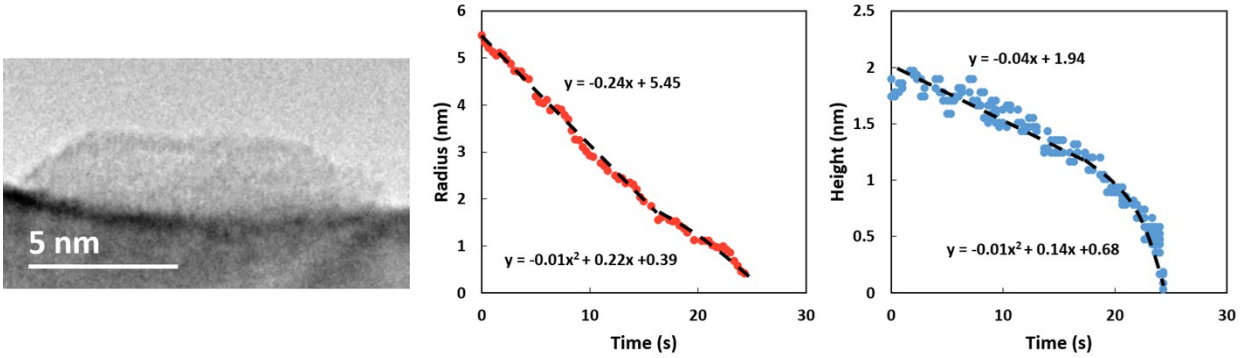

Figure S5. Shrinking profile of Cu_2O island (#5 in Table S8) with fitting parameters.

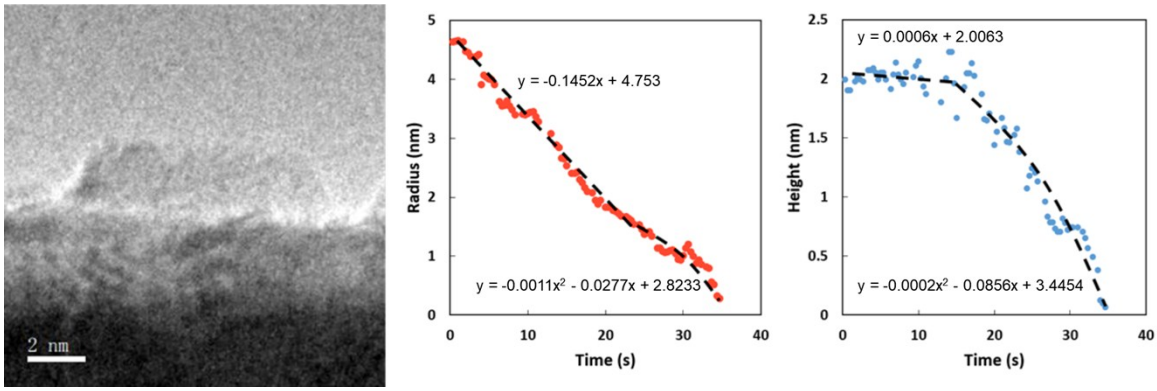

Figure S6. Shrinking profile of Cu_2O island (#6 in Table S8) with fitting parameters.

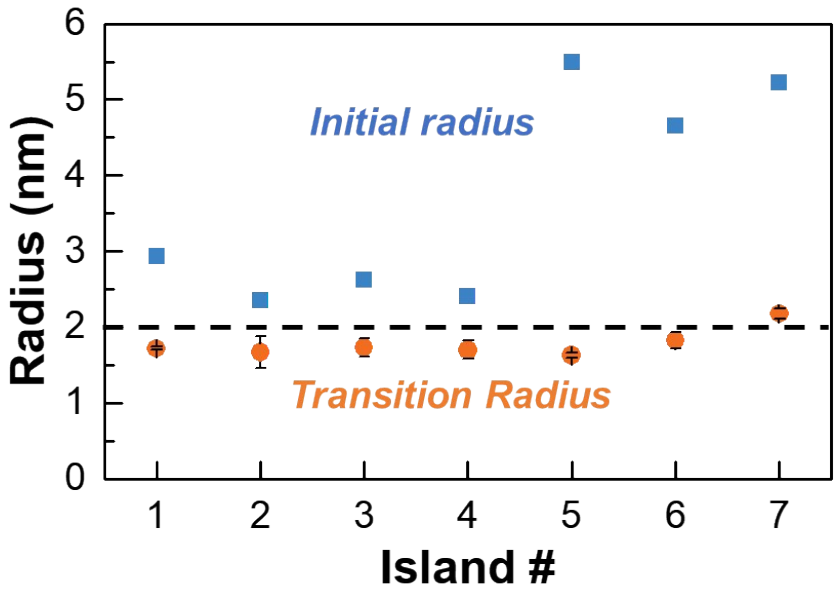

Figure S7. The radii of Cu_2O islands at initial (blue) and transition (orange) stages.

Table S8. Fitted island shrinking rates (linear and parabolic) for radius and height, with transition island dimensions between both shrinking regimes (note that island #7 refers to the island found in the main document of this work). Given the general relationship for fitting shrinking rates $D = At^2 + Bt + C$ (D = dimension length; t = time; A, B, C = fitted coefficients), linear and parabolic rates are respectively defined using the coefficients B (with $A = 0$) and A.

Island #	Linear Shrinking Rate (nm/s × 10^3)		Parabolic Shrinking Rate (nm/s^2 × 10^3)		Initial Dimension (nm)		Transition Dimension (nm)	
	$R_{r,l}$	$R_{h,l}$	$R_{r,p}$	$R_{h,p}$	r	h	r	h
1	-22.3±0.22	-0.420±0.41	-6.23±0.61	-2.73±0.37	2.94	1.40	1.72±0.02	1.30±0.06
2	-12.2±0.19	-2.19±0.14	-0.450±0.02	-1.14±0.02	2.35	1.92	1.67±0.21	1.54±0.22
3	-31.3±1.21	-0.910±0.66	-7.01±2.63	-4.81±0.24	2.62	1.61	1.73±0.12	1.43±0.12
4	-24.7±1.25	-0.230±0.19	-0.680±0.03	-0.270±0.05	2.41	1.88	1.70±0.12	1.81±0.04
5	-235±2.97	-39.2±2.89	-8.86±4.44	-8.95±3.37	5.49	1.97	1.63±0.03	1.36±0.21
6	-145±1.80	-0.639±0.54	-1.11±0.08	-2.17±0.07	4.66	2.14	1.83±0.11	2.08±0.05
7	-142±1.55	-14.7±1.94	-15.3±1.85	-9.10±2.36	5.22	2.36	2.18±0.07	2.06±0.08

Note 2: Statistical Approach for Identifying Cu_2O Island Shrinking Rate Transitions

As shown in Figures 2, 3, and S1-S6, studied Cu_2O islands shrink over two apparently distinct regimes, the first of which features the anisotropic shrinking of island radius (r) with near-constant island height (h). The subsequent regime shows isotropic, near-uniform shrinking of island radius and height. These two shrinking regimes not only appear to show numerically different island radius and height shrinking rates over time, but also may describe shrinking rates with different functional forms.

In order to verify the existence of numerically distinct shrinking rates in the anisotropic and isotropic shrinking regimes, the presence of breaks in shrinking rates at anisotropic-isotropic shrinking transition points was determined via the Chow test.[1]

The shrinking results from the diffusion of Cu away from oxide and has been modeled as linear decay in past work.[2] More specifically, the present work has modeled Cu dissociation as linear atom loss along single island perimeter dimensions, as well as corresponding shrinking of surface areas along multiple distinct island perimeters. The latter of these descriptions can be equated to parabolic shrinking along single dimensions.[32,33]

As can be calculated from Table S8, the ratio of radial to vertical shrinking rates of the seven islands in the anisotropic regime show a mean of 63.12, a minimum of 5.58, and a maximum of 225.52. Respective isotropic shrinking rate ratios show a mean of 1.41, a minimum of 0.39, and a maximum of 2.52. The much faster reduction of island radius, namely compared to island height reduction, in the anisotropic regime suggests that Cu diffusion occurs predominately along a single dimension (radius). Therefore, anisotropic shrinking will be initially approximated via first-order rate kinetics during the Chow test. In contrast, isotropic Cu diffusion can occur primarily along either the height or the radius of a given island, though all radius vs. height ratios are distinctly closer to unity in the case of isotropic (versus anisotropic) shrinking. In this case, either first-order, second-order, or mixed-order (combined first and second) rate kinetics may describe Cu diffusion, depending on the proportions of island shrinking along radius and height. For the purposes of determining the significance of the break between anisotropic and isotropic rates of shrinking within the limitations of the Chow test,[1,2] isotropic shrinking will be initially evaluated using first-order rate kinetics. Nevertheless, future analysis within this Supporting Information will seek to determine whether other kinetics models describe isotropic shrinking more effectively.

Consistent with the assumptions and approximations made above and in past work, the shrinking of oxide islands can be modeled using the following reaction:[3]

$$Cu_2O + 2CH_3OH \rightarrow 2Cu^0 + 2CH_3O + H_2O \quad [1]$$

The methanol decomposition component of this reaction can be stated to explicitly indicate the production of O:

$$2CH_3OH \rightarrow 2CH_3O + 2H \quad [2]$$
$$2H + O \rightarrow H_2O \quad [3]$$

Combination of [1], [2], and [3] ([1] - [2] - [3]) yields the reaction shown in past work:[2]

$$Cu_2O \rightarrow 2Cu^0 + O \quad [4]$$

Applying reaction [4] and first-order rate kinetics to anisotropic ($rate_a = k_a[Cu]$) and isotropic ($rate_i = k_i[Cu]$) island shrinking as tentative approximations, two linear regression models can be derived from given rate equations for the Chow test as follows:

$$r_j = \frac{d[Cu]}{dt} = k_j[Cu] \mid j = a\ (anisotropic)\ OR\ i\ (isotropic)$$

$$\frac{d[Cu]}{[Cu]} = k_j dt \rightarrow \ln([Cu]) = -k_j t + ln([Cu]_0)$$

$$y_j = \ln([Cu])_{t,j} \mid y_{0,j} = \ln([Cu]_0)_j \mid x_{t,j} = t \rightarrow y_{t,j} = -k_j x_{t,j} + y_{0,j} + \varepsilon$$

The Chow test evaluates the Sums of Squared Residuals (SSR) of both combined (a + i) and separate (a, i) anisotropic and isotropic shrinking measurement regressions. Given respective sample sizes N_a and N_i, as well as the number of parameters tested (k), the Chow test inferentially evaluates whether the two regressions depicted above are equivalent using the null hypothesis (H_0), alternate hypothesis (H_A), and F-statistic shown below[1]. Atom concentration ([Cu]) is transformed to a 1-D length scale (e.g.: perimeter) mapped to either island radius or height (l = r *or* h), given the previously described linear decay model. Under this transformation, rate constants (k_j) measuring concentration changes over time are transformed to measure changes in length scale over time (i.e.: dl/dt):[2]

$$H_0: l_{t=0,a} = l_{t=0,i}\ AND\ (dl/dt)_a = (dl/dt)_i$$

$$H_A: l_{t=0,a} \neq l_{t=0,i}\ AND/OR\ (dl/dt)_a \neq (dl/dt)_i$$

$$F = \frac{\left[SSR_{a+i} - (SSR_a + SSR_i)\right]/k}{(SSR_a + SSR_i)/(N_a + N_i - 2k)}$$

For these calculations, note that the breakpoints or transition points defining the anisotropic and isotropic regimes were taken from Table S8 and derived using the Levenberg-Marquardt (LM) Algorithm and piecewise function analysis routines of the Origin software.[4] Results presented below were achieved using the "gap" and "nortest" packages of the R statistical software.[5]

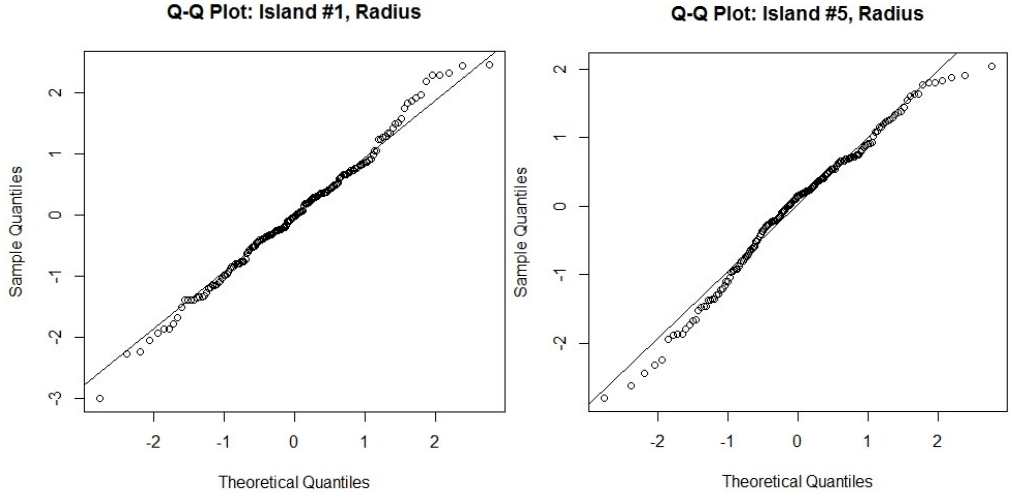

Figure S9. Sample Quantile-Quantile (Q-Q) plots depicting the normality of the regression residuals (ε) of island (#1 and #4) radii shrinking in anisotropic regimes.

The Chow test assumes that regression residuals (ε) are independently and identically distributed from a normal distribution.[1] A representative illustration of the normality of sample regression residuals, which is shown in Figure S9 in Quantile-Quantile (Q-Q) plots, indicates that sample deviations from a normal distribution – or deviations from the 45° degree lines in plotted data – occur almost entirely in ranges of

data more than one quantile away from fitted regression results and at sparsely sampled distances from those results. The Shapiro-Wilk test results of island #1 (p-value = 0.299), which is representative of the majority of sampled islands, and island #4 (p-value = 0.057) show that rejecting the overarching assumption of regression residual normality under a quantitative premise can only occur by using a large significance level (such as $\alpha = 0.1$).[6] In combination, these Q-Q and Shapiro-Wilk results indicate that pertinent data is normally distributed or approximates being normally distributed to the extent of not impeding Chow test evaluations, given that Chow test p-values are sufficiently lower than typically given significance levels (such as $\alpha = 0.05$).[1]

As can be shown in Table S10 below, Chow test results for each island (1-7) and both its radius (r) and height (h) dimensions reveal that the null hypothesis can be strongly rejected for all sampled islands. This can be concluded by using the previously defined significance level ($\alpha = 0.05$) and observing that the largest p-value listed below is distinctly less than this (4.51×10^{-15}). Therefore, distinct anisotropic and isotropic regimes and normality assumptions are statistically justified for the analysis completed in this paper, considering the very low magnitude of all p-values evaluated and the further statistical evaluation of this data completed after Table S10.

Table S10. F-test, degree of freedom, and p-value outputs from Chow tests for each island and shrinking dimension over both anisotropic and isotropic regimes.

Island #	Dimension	*F*-value	$N_a + N_i - 2k$	*p*-value
1	r	255.	216	1.26×10^{-57}
2	r	104.	551	6.75×10^{-39}
3	r	269.	97	2.81×10^{-40}
4	r	300.	346	3.23×10^{-76}
5	r	81.3	61	6.23×10^{-18}
6	r	58.9	82	1.36×10^{-16}
7	r	152.	102	2.54×10^{-31}
1	h	384.	280	5.90×10^{-81}
2	h	507.	527	1.42×10^{-123}
3	h	238.	90	1.11×10^{-36}
4	h	1080	280	3.70×10^{-132}
5	h	60.2	60	4.51×10^{-15}
6	h	183.	74	2.29×10^{-29}
7	h	483.	51	7.04×10^{-34}

In order to evaluate whether isotropic shrinking is characteristic of first or mixed-order (first and second order with mostly second order contributions) rate kinetics, the Akaike Information Criterion (AIC) of each system is resolved.[7] Relative AIC (ΔAIC) values evaluate the trade-off between the inclusion of additional parameters to different models and the minimization of their errors, determining whether the information loss observed by different kinetic models can justify the subtraction of terms from them. Lower ΔAIC values comparing different kinetic models sharing the same data set indicate better model quality with respect to their ordering and their relative magnitudes.[8,9] Through the analysis performed below, the AIC of parabolic (mixed/second order) decay models without two distinct anisotropic and isotropic rates (P), linear decay models with two distinct rates (L+L), and a model with anisotropic linear decay and isotropic parabolic decay (L+P) are compared. Therefore, this analysis determines whether the

addition of parameters required to distinguish two separate rates from one another is justified relative to error reduction, as well as whether error is best minimized by applying first or mixed/second order rate kinetics to the isotropic regime. Also note that, given AIC orderings and relative AIC magnitudes of P, L+L, and L+P models of the same shrinking data are being compared, relative results will not vary with monotonic logarithmic transformations of data. AIC results are summarized in Table S11 below.

Table S11. Differences in AIC results between P, L+L, and L+P models for *r* and *h* of each island over both anisotropic and isotropic regimes. The red, yellow and green shading corresponds to highest, intermediate and lowest ΔAIC values respectively.

Island #	Dimension	ΔAIC (P)	ΔAIC (L+L)	ΔAIC (L+P)
1	r	662	6.02	0.00
1	h	242	10.9	0.00
2	r	986	39.9	0.00
2	h	1790	373	0.00
3	r	89.0	0.00	4.63
3	h	237	46.5	0.00
4	r	317	84.2	0.00
4	h	320	23.7	0.00
5	r	8.44	2.54	0.00
5	h	1.77	8.60	0.00
6	r	86.5	1.84	0.00
6	h	166	4.37	0.00
7	r	542	113	0.00
7	h	95.8	2.36	0.00

As shown in Table S11, L+P models are almost universally favored over L+L and P models, while L+L models are almost universally favored over P models. Given the relative magnitudes of differences between L+P and L+L models, as well as those between L+L and P models, distinguishing between two kinetic rates is very strongly preferred (L+L or L+P) over not doing so (P). In other words, L-P/L-L differences are much smaller than L-L/P differences, frequently by an order of magnitude. Therefore, the two-stage mechanism proposed in this work is both inferentially and informationally justified in a statistical context, given the decay model established in past work shows that L+P models should be used over L+L models in isotropic shrinking over surface areas.[2] Also relative to these differences, exceptions to the general conclusions presented previously occur due to slight differences comparable in size to smaller L-P/L-L differences. Therefore, small quantities of these results can be classified as outliers.

Overall, these results numerically support both the presence of two distinct regimes as well as that first-order rate kinetics describe the anisotropic regime and mixed/second order rate kinetics describe the isotropic regime.

Note 3: Further Computational Details for DFT Calculations

Density Functional Theory (DFT) calculation results featured in this work were achieved using the Vienna *Ab Initio* Simulation Package (VASP, version 5.4.4).[10,11] These calculations applied the Perdew Burke Ernzerhof (PBE) functional,[12] an electronic self-consistent loop break condition of $5x10^{-5}$ eV, and an ionic relaxation loop break condition of 0.02 eV/Å. Projector Augmented Wave (PAW) method resolved pseudopotentials for Cu, O, C, and H elements were used, namely those respectively labelled "Cu", "O_s", "C_s", and "H".[13] The modeling of MeOH adsorption on Cu_2O interfaces, as well as the subsequent MeOH dissociation to form MeO and H adsorbates, was completed using the Climbing-Image Nudged Elastic Band (CI-NEB) method,[14,15] with each CI-NEB calculation employing five images. DFT energetic comparisons were made between structures modeling flat $Cu_2O(100)$ surfaces and stepped $Cu_2O(100)$ interfaces with {100} oriented facets, which most closely resembled experimental structures.[16,17] Modeled structures tested Cu and O terminated surfaces to consider a broader set of O surface coverage conditions.[18] Selective dynamics were used to constrain the bottom half of the flat surface constituting both flat and stepped structures, as well as constrain the columns of atoms perpendicularly intersecting the top flat surfaces of stepped $Cu_2O(100)$ structures.

Initial determinations of energetically favorable candidates for MeOH adsorption and dissociation calculations were made using DFT calculations to screen for the most energetically stable dissociated (MeO and H adsorbates) Cu_2O surface structures that resembled the stepped and flat surfaces resolved in experiment. Pursuant to this screening, stepped $Cu_2O(100)\{100\}$ structures were evaluated, in accompaniment with complementary flat $Cu_2O(100)$ structures, while considering both Cu-terminated and O-terminated surfaces. Energetic results achieved during this screening used an energy cutoff (ENCUT) of 300 eV and were sampled only at the Γ-point (1x1x1 *k*-point grid). Calculations of MeO+H adsorption energies (after dissociated of adsorbed MeOH) were achieved using the expression below, with MeOH molecular energies determined using the convergence of similarly parameterized calculations with increasing box size (up to 12 Å x 12 Å x 12 Å):

$$E_{ads} \equiv \Delta E = E_{MeO+H} - (E_{MeOH} + E_{Cu2O})$$

Using the above notation, MeO+H adsorption energies following dissociation (ΔE, defining E_{ads} in the main document) are calculated from the DFT energies of simulations featuring separate adsorption of MeO and H adsorbates on a given Cu_2O interface (E_{MeO+H}), an isolated MeOH molecule (E_{MeOH}), and a corresponding Cu_2O interface calculation without any adsorbates (E_{Cu2O}). MeOH adsorption energy screening results for flat $Cu_2O(100)$ surfaces are summarily depicted for both Cu and O-terminated structures in Figure S12 below. Note that, in all structures visualized in future figures, Cu, O, C, and H atoms are respectively represented as blue, red, brown, and white spheres using the VESTA software package.[19]

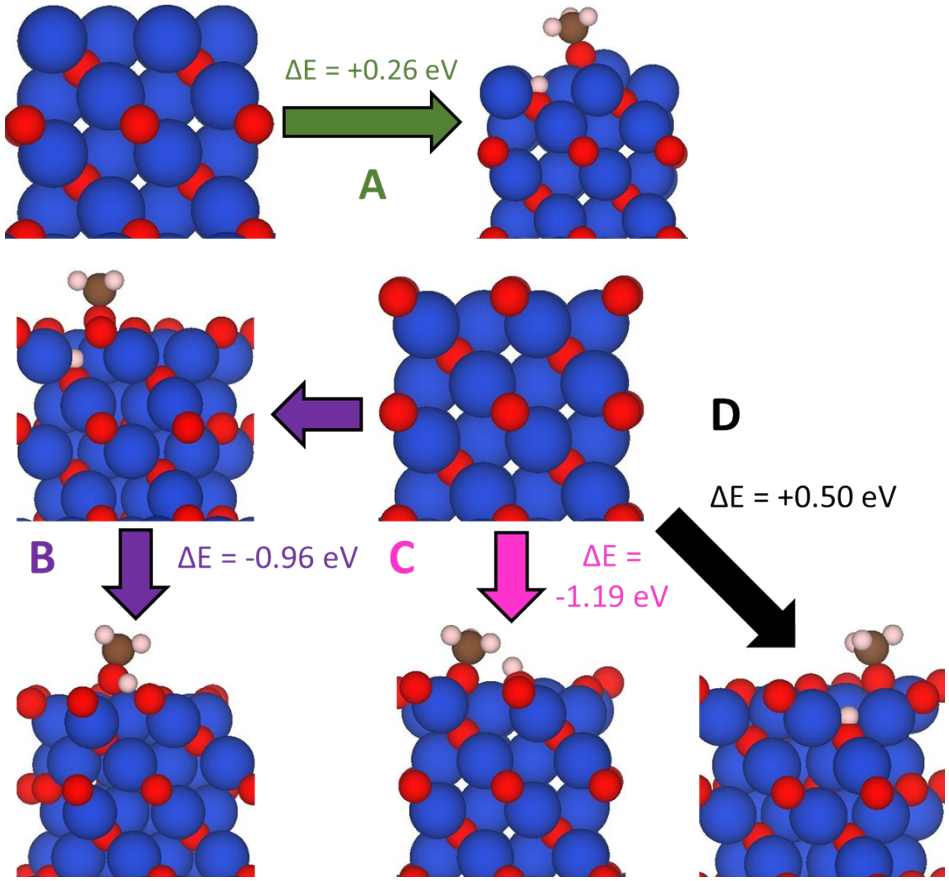

Figure S12. Flat $Cu_2O(100)$ Cu(A) and O-terminated(B, C, D) structures with MeOH adsorption energetics after dissociation of H to surface (B, C) and lattice (D) O sites.

Over all structures evaluated, note that the O atoms of MeO adsorbates initially had two-fold coordination, as each of them was most closely attached to single C and Cu atoms. In the case of the Cu-terminated flat $Cu_2O(100)$ surface (Figure S12A), only lattice or subsurface O atoms can bond to H atoms. Given that subsurface O atoms serve as nearly structurally equivalent sites for H adsorption from MeOH dissociation due to being in Cu surrounded environments, only the O atom nearest to the H atoms was tested. Relaxation of the MeO adsorbate upon dissociation yielded an adsorbed O with three-fold coordination (Cu, Cu, C) and a relatively high adsorption energy (ΔE_{S12A} = +0.23 eV). This relaxation to three-fold coordination leads to a structure in which MeO adsorbates are located near singularly coordinated (equivalent) H adsorbate sites, further justifying past testing of only nearest neighbor sites.

Subsequently tested O-terminated flat $Cu_2O(100)$ surfaces (Figure S12B, S12C, S12D) initially evaluated four structures systematically, featuring H adsorbing to a nearest neighbor surface O (Figure S12C), nearest neighbor subsurface O, next nearest neighbor surface O (Figure S12B), and next nearest neighbor subsurface O (Figure S12D). The initial structure used to initialize the relaxed structure depicted in Figure S12B placed an H adsorbate on the nearest neighbor subsurface O, which then relaxed into a structure (Figure S12B) placing an H atom at an intermediate distance between the MeO adsorbate and the next nearest neighbor surface O adsorption site. Subsequent evaluations revealed that the most energetically favorable structure tested adsorbs H at the nearest neighbor surface O site (Figure S12C) and the least favorable stable structure adsorbs H at the next nearest neighbor subsurface O site. Consistent with previous calculations, MeOH dissociation to MeO leads to a transition from two-fold to three-fold coordination during MeO+H relaxation. Also consistent with past work,[20,21] flat O-terminated surfaces are shown to much more (1.45 eV) favorably adsorb and dissociate MeOH.

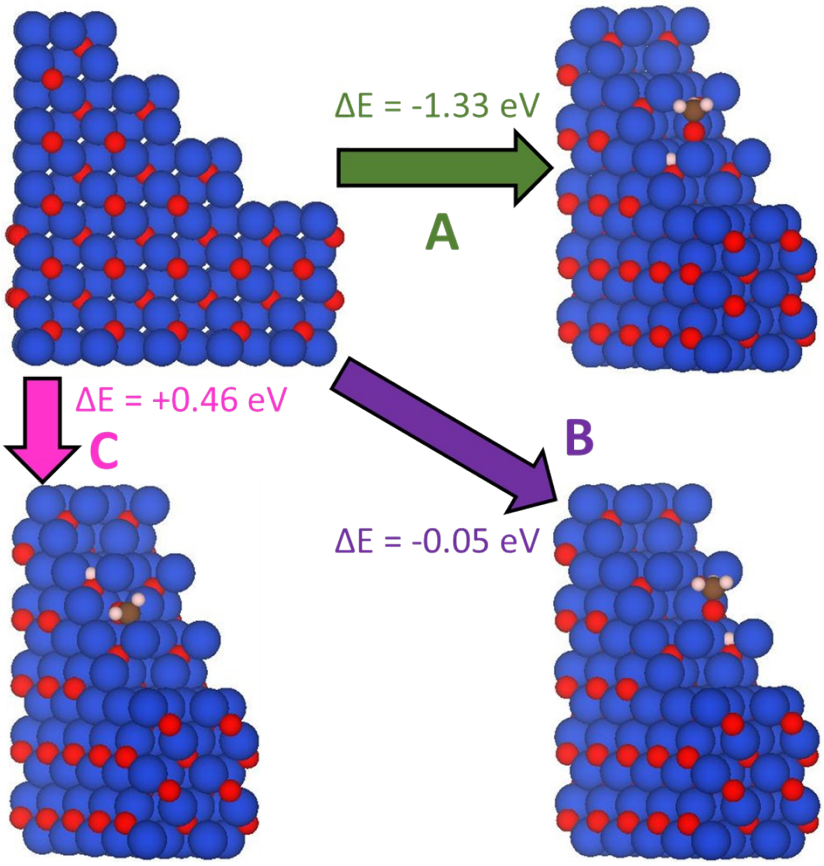

Figure S13. $Cu_2O(100)\{100\}$ Cu-terminated stepped surfaces with MeOH adsorption and dissociation, with MeO adsorption on (A)step edges adjacent to H adsorbates, (B) flat surfaces shared by H adsorbates, (C) flat surfaces adjacent to H adsorbates.

Cu-terminated $Cu_2O(100)\{110\}$ interfaces depict several sites for MeO and H dissociative adsorption that can be distinguished from one another based on the locations of MeO and H relative to one another. Given that O within Cu-terminated Cu_2O steps is solely located in the subsurface of the Cu_2O step, MeO adsorbate positions are limited to allow diffusion of H from MeOH to subsurface O in single linear paths.[22] From this limitation, three distinct structures are readily defined and tested as candidates for MeOH dissociation, including MeO adsorbed to a {100} step edge adjacent to a complementary H adsorbate (Figure S14A). Additionally, MeO can be adsorbed to a flat surface adjacent to an H adsorbate on a shared (Figure S14B) or adjacent (Figure S14C) flat surface. In each of these cases, initial two-fold coordination was given to MeO adsorbates, though relaxation generally led to MeO assuming three-fold coordination. Over these cases, MeO adsorbing on the step edge (Figure S14A) is shown to be most energetically favorable.

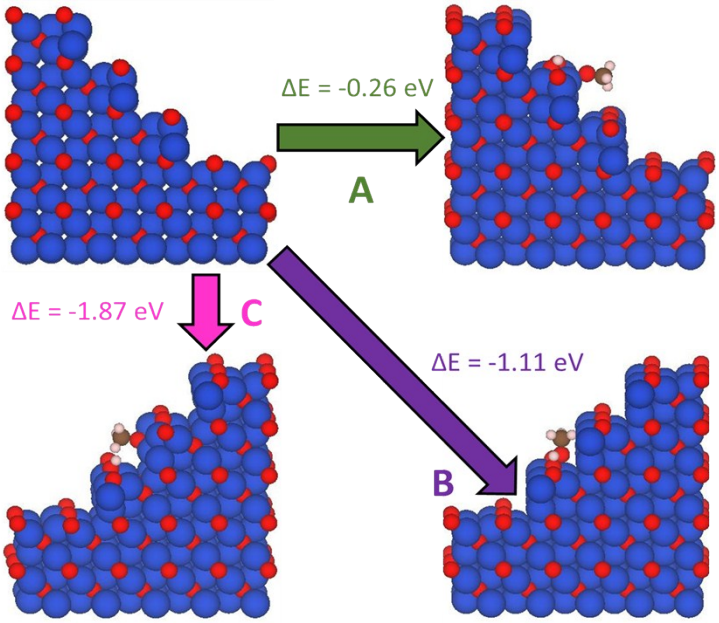

Figure S14. $Cu_2O(100)\{100\}$ O-terminated (O bonded to step edge) stepped surfaces with MeO adsorption on shared(A) and adjacent(C) step edges as H adsorbates, as well as MeO adsorption on flat surfaces shared by H adsorbates(B).

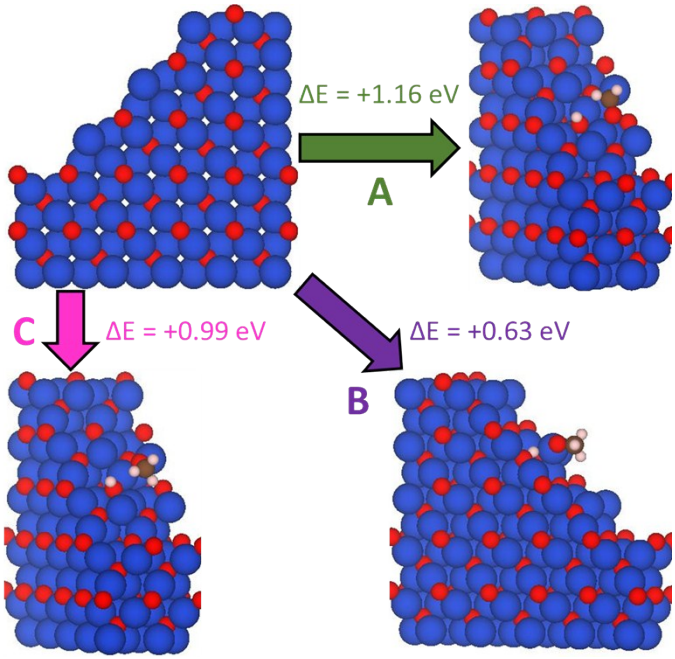

Figure S15. $Cu_2O(100)\{100\}$ O-terminated (O not bonded to step edge) stepped surfaces with MeO adsorption on shared (B) and adjacent (C) step edges as H adsorbates, as well as MeO adsorption on flat surfaces shared by H adsorbates (A).

Figures S14 and S15 both depict $Cu_2O(100)\{100\}$ structures with O-terminations. However, the 6 atom P*n*-3*m* Cu_2O unit cell used for constructing all flat and stepped surfaces contains two O atoms, which are symmetrically equivalent in bulk, that become symmetrically inequivalent when forming stepped

$Cu_2O(100)$ surfaces.[23] Figure S14 depicts MeO and H adsorption on O-terminated structures with O bonded to the Cu atoms forming a step edge, while Figure S15 shows structures with O bonded to Cu forming the flat surfaces connecting these steps. Upon evaluation, all structures tested in Figure S14 are found to be more favorable than those in Figure S15, thus further analysis of Figure S15 will not be completed. In all cases, structures were initialized by applying two-fold coordination to the O of adsorbed MeO.

Applying screening criteria similar to those used to test MeO and H adsorption sites in Figure S14, tested structures include MeO on steps shared by (Figure S15A) and adjacent to (Figure S15C) adsorbed H, with MeO adsorbed to two-fold coordinate Cu atoms forming step edges. Another structure tests MeO adsorbed to a three-fold coordinate Cu forming a flat surface (Figure S15B), which is on the same surface as an adsorbed H. The most favorable structure, depicted in Figure S15C, features relaxation of a MeO adsorbate with initial two-fold O coordination to three-fold O coordination, consistent with past test results.

The testing of structures shown above constitutes the screening of Cu and O-terminated $Cu_2O(100)$ and $Cu_2O(100)\{100\}$ surfaces needed to select candidates for evaluating disproportionate adsorption energetics, which can be linked to anisotropic island shrinking. In summary, the screening of Cu and O-terminated $Cu_2O(100)$ and $Cu_2O(100)\{100\}$ interfaces revealed that O-terminated structures are more favorable than Cu-terminated structures overall. Additionally, adsorbate configurations on the most favorable structures were shown to initialize O (in MeOH) with two-fold coordination and subsequently relax to yield O (in MeO) with three-fold coordination primarily affected by additional Cu-O bonding. $Cu_2O(100)\{100\}$ structures proving more favorable than the most favorable $Cu_2O(100)$ flat surface adsorbate configurations (-1.19 eV) always featured MeO adsorption on relatively undercoordinated step edge sites, consistent with experimental expectations for anisotropic island shrinking. Furthermore, the most favorable $Cu_2O(100)\{100\}$ structure resolved observed MeO and H adsorbates on adjacent edge sites. Therefore, the structures selected as candidates for Figure 4, namely from evaluations performed via Figures S12-S15, are shown in Figure S12C and Figure S14C for $Cu_2O(100)$ and $Cu_2O(100)\{100\}$ systems, respectively.

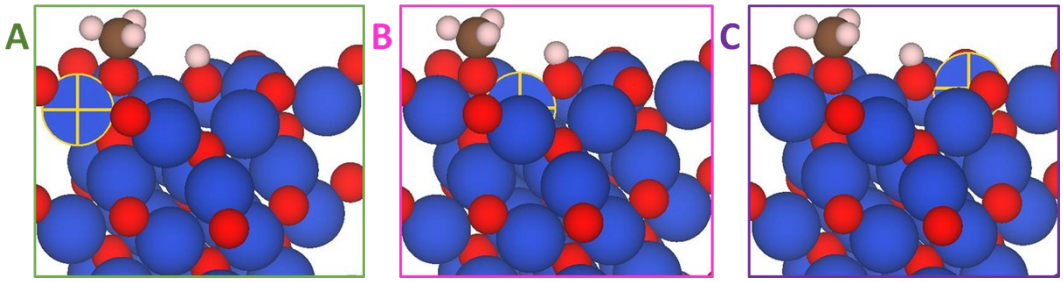

Figure S16. Tested Cu sites – labelled MeO(A), MeO-H(B), and H(C) – for Hubbard U linear response calculations, spanning the H diffusion path of MeOH dissociation.

Evaluation of the effects of electronic correlation starts with the calculation of Hubbard U (U_{3d}) parameters using a linear response approach on pertinent Cu atoms of evaluated structures. Preliminary relaxation and linear response calculations are completed by applying an energy cutoff (ENCUT) of 550 eV and calculation parameters otherwise matching those used in previous test calculations. Linear response techniques employed in past work[24,25] were first applied to the most favorable flat $Cu_2O(100)$ system (Figure S12C), using a 4x4x1 Γ-point centered grid. Linear response calculations are applied to Cu sites over which H diffuses from MeO to next nearest neighbor O adsorbates, given that these Cu sites are closest to the dissociation processes being modeled. As depicted in Figure S16, Cu sites nearest MeO,

between MeO and H, and nearest H adsorbates are calculated to have Hubbard U values of 8.81 ± 0.49 eV, 9.84 ± 0.60 eV, and 8.78 ± 0.54 eV, respectively. Validation for these results is provided by calculation of the Hubbard U values for bulk $CuCO_3$ and CuH_2O_2 systems, which respectively model Cu-O-C and Cu-O-H bonding and were resolved from OQMD.[23] Using respective 2x2x2 (40 atoms) and 1x2x1 (20 atoms) supercells based on 8x8x8 Γ-point centered grid scaled for dimensions, respective Hubbard U values of 10.30 ± 0.50 eV and 10.14 ± 0.50 eV values were calculated for the systems shown in Figure S17.

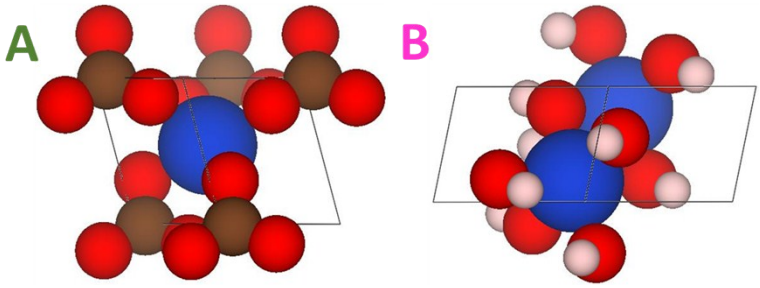

Figure S17. Unit cell representations of bulk $CuCO_3$ (A) and CuH_2O_2 (B) structures.

Given the Hubbard U values and their respective overlapping uncertainties, a single Hubbard U value of 9.3 eV was used to model all MeOH adsorption and dissociation processes involving electronic correlation in this work. Considering that the undercoordination of metal cations has been shown to produce changes in calculated linear response U values of ~0.5 eV,[26] $CuCO_3$ and CuH_2O_2 can be equated to the previously calculated 9.3 eV result within uncertainty and other considerations. Reviewing the effects of surface undercoordination on calculated U values, this result is consistent with a similar Hubbard U value (10 eV), which was calculated from fitting the band gap of bulk Cu_2O, applied to ethanol adsorption on Cu_2O(111) surfaces.[26,27]

Final results comparing the most favorable flat surface (Figure S12C) to the most favorable stepped surface (Figure S15C) are displayed in Figure 4. Adsorption and diffusion energetics resolved in these sections apply an energy cutoff (ENCUT) of 400 eV, a Monkhorst-Pack *k*-point grid of 2x2x1,[28] the DFT-D3 Grimme method for modeling dispersion effects,[29] the Dudarev implementation of the Hubbard U method,[30] and otherwise matching criteria compared to what was described previously. Including DFT-D3 in Hubbard U linear response calculations had effects (~0.1 eV) on those results that were well within reported uncertainties.

For all interfacial systems calculated in this section, diffusion energies (E_{diff}) were calculated from a starting structure featuring MeO and H adsorbates and two-fold O coordination (Cu, C), while leading to a terminal structure with three-fold O coordination (Cu, Cu, C) and both MeO and H adsorbates. The E_{diff} result calculated for MeOH dissociation on the most favorable flat Cu_2O(100) surface (0.25 eV) is strongly consistent with the most favorable barriers associated with MeOH diffusion processes on Cu_2O(111) in past work (0.28 eV).[22] Beyond validating prior experimental sections, illustration of the link between adsorption site energetics and island shrinking retroactively validates the sole use of E_{ads} (Figures S12-S17) in screening candidate structures for MeOH adsorption and dissociation.

ESI References

1. Chow GC (1960). Tests of equality between sets of coefficients in two linear regression. *Econometrica* 28:591-605
2. Zhou, G. and J.C. Yang, Reduction of Cu_2O islands grown on a Cu(100) surface through vacuum annealing. Phys Rev Lett, 2004. **93**(22): p. 226101.
3. Bowker, M., Catalysis resolved using scanning tunnelling microscopy. Chem Soc Rev, 2007. **36**(10): p. 1656-73.
4. Origin (OriginLab, Northampton, MA)
5. R Core Team. R: A language and environment for statistical computing. (2013).
6. Shapiro, S. S. and Wilk, M. B. An analysis of variance test for normality (complete samples). *Biometrika* 52.3/4 (1965): 591-611.
7. Akaike, Hirotugu. A new look at the statistical model identification. *IEEE transactions on automatic control* 19.6 (1974): 716-723.
8. Nikolaidis, Georgios, Tobias Baier, Ralf Zapf, Gunther Kolb, Volker Hessel, and Wilhelm F. Maier. "Kinetic study of CO preferential oxidation over Pt–Rh/γ-Al_2O_3 catalyst in a micro-structured recycle reactor." *Catalysis Today* 145, no. 1-2 (2009): 90-100.
9. Koeppenkastrop, D., & De Carlo, E. H. (1993). Uptake of rare earth elements from solution by metal oxides. *Environmental science & technology*, *27*(9), 1796-1802.
10. Kresse, G. and Furthmüller, J., Efficient iterative schemes for *ab initio* total-energy calculations using a plane-wave basis set. *Physical Review B* **1996**, *54* (16), 11169-11186.
11. Kresse, G.; Joubert, D., From ultrasoft pseudopotentials to the projector augmented-wave method. *Physical Review B* **1999**, *59* (3), 1758-1775.
12. Perdew, J. P.; Burke, K.; Ernzerhof, M., Generalized gradient approximation made simple. *Physical Review Letters* **1996**, 77 (18), 3865-3868.
13. Blöchl, P. E., Projector augmented-wave method. *Physical Review B* **1994**, *50* (24), 17953-17979.
14. Henkelman, G.; Jónsson, H., Improved tangent estimate in the nudged elastic band method for finding minimum energy paths and saddle points. *The Journal of Chemical Physics* **2000**, *113* (22), 9978-9985.
15. Henkelman, G.; Uberuaga, B. P.; Jónsson, H., A climbing image nudged elastic band method for finding saddle points and minimum energy paths. *The Journal of Chemical Physics* **2000**, *113* (22), 9901-9904.
16. Zhu, Q.; Saidi, W. A.; Yang, J. C., Step-Edge Directed Metal Oxidation. *The Journal of Physical Chemistry Letters* **2016**, *7* (13), 2530-2536.
17. Zou, L. et al., *In situ atomic-scale imaging of the metal/oxide interfacial transformation.* Nature Communications, 2017. **8**(1): p. 307.
18. Chi, H. et al., *Dependence of H_2 and CO_2 selectivity on Cu oxidation state during partial oxidation of methanol on Cu/ZnO.* Applied Catalysis A: General, 2018. **556**: p. 64-72.
19. Momma, K. and Fujio I. VESTA: a three-dimensional visualization system for electronic and structural analysis. Journal of Applied Crystallography, 2008 41 (3) 653-658.
20. Sakong, S. and A. Gross, Total Oxidation of Methanol on Cu(110): A Density Functional Theory Study. The Journal of Physical Chemistry A, 2007. 111(36): p. 8814-8822.
21. Li, J. and G. Zhou, Density functional theory study of O–H and C–H bond scission of methanol catalyzed by a chemisorbed oxygen layer on Cu(111). Surface Science, 2016. 646: p. 288-297.
22. Riguang, Z., et al., A DFT study on the formation of CH_3O on Cu_2O(111) surface by CH_3OH decomposition in the absence or presence of oxygen. Applied Surface Science, 2011. 257(9): p. 4232-4238.
23. Saal, J. E., Kirklin, S., Aykol, M., Meredig, B., & Wolverton, C. (2013). Materials design and discovery with high-throughput density functional theory: the open quantum materials database (OQMD). *Jom*, *65*(11), 1501-1509.

24. Cococcioni, Matteo, and Stefano De Gironcoli. "Linear response approach to the calculation of the effective interaction parameters in the LDA+ U method." *Physical Review B* 71.3 (2005): 035105.
25. Curnan, Matthew T., and John R. Kitchin. "Effects of concentration, crystal structure, magnetism, and electronic structure method on first-principles oxygen vacancy formation energy trends in perovskites." *The Journal of Physical Chemistry C* 118.49 (2014): 28776-28790.
26. Aschauer, Ulrich, et al. Influence of subsurface defects on the surface reactivity of TiO2: water on anatase (101). *The Journal of Physical Chemistry C* 114.2 (2009): 1278-1284.
27. Xu, H., et al., Mechanism of C-C and C-H bond cleavage in ethanol oxidation reaction on Cu2O(111): a DFT-D and DFT+U study. Physical Chemistry Chemical Physics, 2017. 19(38): p. 26210-26220.
28. Monkhorst, H. J.; Pack, J. D., Special points for Brillouin-zone integrations. *Physical Review B* **1976,** *13* (12), 5188-5192.
29. Grimme, Stefan, et al. "A consistent and accurate ab initio parametrization of density functional dispersion correction (DFT-D) for the 94 elements H-Pu." *The Journal of chemical physics* 132.15 (2010): 154104.
30. Dudarev, S. L., et al. Electron-energy-loss spectra and the structural stability of nickel oxide: An LSDA+ U study. *Physical Review B* 57.3 (1998): 1505.
31. Curnan, M. T. et al., "Connecting Oxide Nucleation and Growth to Oxygen Diffusion Energetics on Stepped Cu(011) Surfaces: An Experimental and Theoretical Study", *The Journal of Physical Chemistry C* 123 (2019): 452-463
32. Tersoff, J. and Tromp, R. M., "Shape Transition in Growth of Strained Islands: Spontaneous Formation of Quantum Wires", *Physics Review Letters* **70** (1993): 2782.
33. Zhou, G. and Yang, J. C., "Formation of Quasi-One-Dimensional Cu_2O Structures by *in situ* Oxidation of Cu(100)", *Physical Review Letters* **89**(10) (2002): 106101